Available online at www.sciencedirect.com

SciVerse ScienceDirect

Geochimica et Cosmochimica Acta 108 (2013) 91–106

Geochimica et Cosmochimica Acta

www.elsevier.com/locate/gca

Magnesite dissolution rates at different spatial scales: The role of mineral spatial distribution and flow velocity

Fatemeh Salehikhoo [a], Li Li [a,c,*], Susan L. Brantley [b,c]

[a] John and Willie Leone Family Department of Energy and Mineral Engineering, The Pennsylvania State University, University Park, PA 16802, United States

[b] Department of Geosciences, The Pennsylvania State University, University Park, PA 16802, United States

[c] Earth and Environmental Systems Institute (EESI), The Pennsylvania State University, University Park, PA 16802, United States

Received 17 January 2012; accepted in revised form 9 January 2013; Available online 24 January 2013

Abstract

We examined the role of mineral spatial distribution and flow velocity in determining magnesite dissolution rates at different spatial scales. One scale is the column scale of a few to tens of centimeters where dissolution rates are measured. Another is the "local" in situ scale defined as approximately 0.1 mm. The experiments used two columns with the same bulk concentration but different spatial distributions of magnesite. In the "Mixed" column, magnesite was evenly distributed spatially within a quartz sand matrix across the whole column, while in the "One-zone" column, magnesite was distributed in one zone in the middle of the column. The two columns were flushed with the same inlet acidic solution (pH 4.0) under flow velocities varying from 0.18 to 36 m/d. Columns of different lengths (22, 10, and 5 cm) were run to understand the role of length scales. Reactive transport modeling was used to infer local-scale and column-scale dissolution rates.

Under the acidic-solution flushing conditions used in this study, local in situ dissolution rates vary by orders of magnitude over a length scale of a few to tens of centimeters. Column-scale rates under different conditions vary between 6.40×10^{-12} and 1.02×10^{-9} mol/m^2/s. The distribution of local-scale rates, which collectively determine the column-scale rates, depend on flow velocity, column length scale, and mineral distribution. A two orders of magnitude difference in flow velocity results in more than two orders of magnitude difference in the column-scale rates. Under the same conditions of flow velocity and mineral distribution, column-scale rates are higher in short columns and are lower in long columns. Mineral spatial distribution made a maximum difference of 14% in the medium-flow velocity regime where the reaction kinetics of the system operates under mixed-control conditions. Under such mixed-control conditions, the larger difference between the two columns in their spatial variation of pH and saturation state lead to a larger difference in the spatial distribution of local dissolution rates and therefore column-scale rates. In contrast, under slow-flow velocity conditions, the system is mostly at equilibrium without much spatial variation, i.e., the regime of local equilibrium. Under fast-flow velocity conditions, the system is kinetically controlled, the local aqueous geochemistry is everywhere similar to the inlet condition, and is also relatively uniform. Under these two conditions, there is almost no difference between the two columns. Column-scale rates were best understood in terms of the Damkohler number (Da_I) that quantifies the relative dominance of advection and dissolution processes. The observations in this study lead us to surmise that rates of weathering and other natural processes may be similarly affected by chemical heterogeneity in natural systems under conditions where reaction rate and flow rate are comparable.

1. INTRODUCTION

Mineral dissolution and precipitation reactions influence many chemical and physical phenomena in earth and environmental sciences (Bain et al., 2001; Steefel et al., 2005;

* Corresponding author at: John and Willie Leone Family Department of Energy and Mineral Engineering, The Pennsylvania State University, University Park, PA 16802, United States. Tel.: +1 814 867 3547; fax: +1 814 865 3248.

E-mail address: lili@eme.psu.edu (L. Li).

0016-7037/$ - see front matter © 2013 Elsevier Ltd. All rights reserved.
http://dx.doi.org/10.1016/j.gca.2013.01.010

Chen et al., 2009; Brantley, 2010; Chang et al., 2011; Frye et al., 2012; Landrot et al., 2012). The rates of mineral dissolution have been extensively investigated in both laboratory experiments and field studies (Chou et al., 1989; Chris, 1993; Gautelier et al., 1999; White and Brantley, 2003; Navarre-Sitchler et al., 2009; Pokrovsky et al., 2009; Jin et al., 2010). Most laboratory studies on mineral dissolution kinetics were carried out in batch or flow-through reactors that are designed to be well-mixed. In contrast, in the field, weathering rates have often been quantified based on observed mineral depletion fronts or water chemistry over meters to kilometers of water flow path (Brimhall and Dietrich, 1987; Casey et al., 1993; Velbel, 1993; Anderson et al., 2002; Maher et al., 2004, 2006; Zhu, 2005; Lebedeva et al., 2007; Navarre-Sitchler and Brantley, 2007; Brantley et al., 2008; White, 2008; Brantley and White, 2009; Zhu, 2009; Jin et al., 2010; Maher, 2010, 2011). Laboratory derived-dissolution rates have in general been found to be one to five orders of magnitude greater than those observed in the field (Swoboda-Colberg and Drever, 1993; White and Brantley, 2003; Maher et al., 2004; Navarre-Sitchler and Brantley, 2007).

A variety of factors have been proposed to explain the discrepancies between laboratory and field rates. These include the differences in the surface area of fresh and weathered minerals (White and Peterson, 1990; Anbeek, 1993; White, 1995), the effect of reaction affinity (White, 1995; White and Brantley, 2003; Maher et al., 2006), the precipitation of secondary minerals (Steefel and Van Cappellen, 1990; Alekseyev et al., 1997; Zhu et al., 2004; Maher et al., 2006, 2009), mineral coatings (Nugent et al., 1998; Hodson, 2003), and the age of the reacting material (White and Brantley, 2003; Maher et al., 2004). Recent interest has focused on the combined effects of affinity, clay precipitation, and residence time in controlling dissolution rates (Maher et al., 2009; Zhu, 2009; Maher, 2010; Moore et al., 2012).

Recent studies have also attributed laboratory-field rate discrepancies to the variation in conditions under which weathering occurs (Malmstrom et al., 2000, 2004; Miralles-Wilhelm and Gelhar, 2000; Wood and Whitaker, 2000; Li et al., 2006; Meile and Tuncay, 2006; Song and Seagren, 2008). Dissolution processes under natural conditions are often coupled with flow and transport processes and can be influenced by an array of different factors when considered at different scales. The natural subsurface is inherently heterogeneous in terms of its spatial distribution of physical and chemical properties. Physical properties such as permeability often vary by orders of magnitude and therefore lead to large variations in flow velocities and therefore residence time (Freeze and Cherry, 1979; Newell et al., 1990; Rubin and Gomez-Hernandez, 1990; Gelhar et al., 1992; Gelhar, 1993; Fetter, 1999; Hubbard and Rubin, 2000; Chen et al., 2001; Maher, 2010; Li et al., 2011). Minerals are unevenly distributed, which can result in local geochemical conditions that differ significantly from observations at larger spatial scales (Wilkin et al., 1996; Noiriel et al., 2007; Peters, 2009; Li et al., 2010, 2011). All these can affect the relative rate of mass transport and dissolution rates at different spatial scales.

Physical heterogeneities have long been known to affect flow and transport processes (Freeze, 1975; Gelhar and Axness, 1983; Dagan, 1990; Gelhar et al., 1992; Gelhar, 1993; Berkowitz, 2002; Zinn et al., 2004; Knutson et al., 2005, 2007; Werth et al., 2006; Cirpka and Valocchi, 2007; Cirpka et al., 2008; Willingham et al., 2008; Castro-Alcala et al., 2012). The effect of geochemical heterogeneities, however, have been investigated to a much lesser extent (Tompson et al., 1996; Glassley et al., 2002; Dentz et al., 2004, 2011a,b; Li et al., 2006, 2007a,b, 2010, 2011; Meile and Tuncay, 2006; Scheibe et al., 2006; Cirpka et al., 2008). Li and co-workers used pore-scale network modeling to show the importance of spatial mineral distribution in determining the extent of mixing and overall reaction rates at the continuum scale (Li et al., 2006, 2007b,c). At relatively small scales, for example, at the pore scale, the local-scale dissolution rates are a function of local aqueous geochemistry conditions dictated by local mineral spatial patterns and heterogeneities (Landrot et al., 2012; Molins et al., 2012). The dissolution rates at larger spatial scales are collectively determined by averaging over local-scale dissolution rates (Li et al., 2006, 2008; Navarre-Sitchler and Brantley, 2007; Molins et al., 2012). As a result, with the same total amount of reactive minerals, different mineral spatial distribution leads to differing rates at the pore network scale. At the scale of tens of meters, Li et al. (2010, 2011) have also studied the importance of geochemical and physical heterogeneity in determining uranium bioreduction rates. However, no systematic experimental work has explored the effects of heterogeneities in controlling mineral dissolution rates from the geochemical perspective.

The effect of flow and transport on mineral reaction rates has been discussed in the context of transport- versus surface-controlled reaction kinetics (Berner, 1978; Dibble and Tiller, 1981; Rickard and Sjoberg, 1983; Sjoberg and Rickard, 1983; Casey, 1987; Murphy et al., 1989; Schnoor, 1990; Kump et al., 2000; Li et al., 2007a,c, 2008, 2011a; Lebedeva et al., 2010; Maher, 2010). Both field data and well-mixed laboratory experiments suggest that the reaction rates under different flow velocity regimes can vary significantly. For example, Schnoor (1990) argued that Si release rate in field systems (equated to weathering rate) increases to a maximum value that is comparable to release rates measured in silicate dissolution rates in the laboratory as the soil flushing rate increases. Maher (2010) shows order of magnitude changes in weathering rates as a function of flow rate, emphasizing the significant hydrologic controls on weathering rates. Through modeling studies, Li et al. (2007a) has shown that flow velocities can determine the importance of chemical heterogeneities in controlling anorthite dissolution rates. A few researchers also have investigated the effect of stirring on mineral kinetics (Rickard and Sjoberg, 1983; Sjoberg and Rickard, 1983; Rosso and Rimstidt, 2000). However, the experimental work has mainly focused on effects of stirring rates on dissolution rates in well-mixed batch reactors. Systematic experimental studies on the role of flow velocities in determining mineral dissolution rates have rarely been carried out at different spatial scales and under conditions similar to natural

weathering conditions where advection, dispersion/diffusion, and reaction processes are coupled.

The goal of this work is to understand and to quantify the role of mineral spatial distribution and flow velocity in determining the magnesite dissolution rate measured at different spatial scales. One scale we consider is the column scale, i.e., the spatial scale of a few to tens of centimeters where dissolution rates are measured. Another scale is the spatial scale of approximately 0.1 mm, the "local" in situ scale. We use numerical simulation to understand rates at the spatial scale that is relevant to the size of grid blocks. We investigate the magnesite dissolution rates in two columns. One is the "Mixed" column in which the magnesite is distributed evenly within a quartz sand column, while the other is the "One-zone" column in which the magnesite grains are distributed as a single zone in the middle of the quartz sand column. The two columns have the same physical properties and total amount of magnesite. This experiment is a model for natural systems where different types of minerals are often distributed in different patterns. The two columns were run under the flow velocities of 0.18 to 36 m/d and under three column length scales (22, 10, and 5 cm). With the advantage of well-controlled column experiments and the coupled reactive transport modeling, we aim to quantify dissolution rates at the local scale and the column scale, and to understand key controls of magnesite dissolution rates under an array of flow and transport conditions.

2. MAGNESITE DISSOLUTION RATES IN WELL-MIXED REACTORS

Magnesite is chosen because it is a carbonate mineral and has been extensively studied in well-mixed batch reactors (Morse and Arvidson, 2002; Saldi et al., 2009). Carbonate minerals are commonly found in sedimentary rocks and sediments (Morse and Arvidson, 2002; Morse et al., 2007) and are important minerals during geological CO_2 sequestration and many other applications. Magnesite dissolution kinetics have been documented extensively (Chou et al., 1989; Luttge et al., 1999; Luttge, 2005; Pokrovsky et al., 2005; Luttge and Arvidson, 2008; Pokrovsky et al., 2009; Saldi et al., 2010). Although the work of Pokrovsky and others has emphasized surface complexation reactions in determining magnesite dissolution, we use here the older rate laws based entirely on solution chemistry. Specifically, we use the three different parallel reactions for magnesite dissolution kinetics as proposed in the literature (Plummer and Wigley, 1976; Chou et al., 1989):

$$MgCO_3(s) + H^+ \rightleftharpoons Mg^{2+} + HCO_3^- \quad (1)$$

$$MgCO_3(s) + H_2CO_3^* \rightleftharpoons Mg^{2+} + 2HCO_3^- \quad (2)$$

$$MgCO_3(s) \rightleftharpoons Mg^{2+} + CO_3^{2-} \quad (3)$$

We modeled the reactions using a Transition State Theory (TST) based rate law:

$$r_{MgCO_3} = (k_1 a_{H^+} + k_2 a_{H_2CO_3^*} + k_3)\left(1 - \frac{IAP}{K_{eq}}\right). \quad (4)$$

Here k_1, k_2, and k_3 are the rate constants (mol m^{-2} s^{-1}), a_{H^+} and $a_{H_2CO_3^*}$ are the activities of hydrogen ion and carbonic acid (unitless). The ion activity product (IAP) is defined as $a_{Mg^{2+}} a_{CO_3^{2-}}$, and K_{eq} is the equilibrium constant for Reaction (3). Although reactions (1) to (3) have different IAP and K_{eq} values, it can be easily proved that the value of IAP/K_{eq} is the same for all three reactions by explicitly writing the IAP/K_{eq} expressions for all three reaction pathways. The rate law (Eq. (4)) reveals that magnesite reaction rates depend on mineral reactivity, surface area, and aqueous geochemistry, including pH and deviation from equilibrium.

3. METHODOLOGY

In this work, effluent magnesium concentrations from column experiments were used to determine overall integrated dissolution rates at the column scale. Reactive transport modeling was used to match column experimental effluent data and to infer local "in situ" rates in each grid block.

3.1. Column experiments

3.1.1. Material preparation

The magnesite was a natural sample in a private collection obtained from Mongolia. X-ray diffraction analysis of the sample indicated that magnesite is the only detectable crystalline phase. Consistent with this, bulk analysis using inductively coupled plasma emission spectrometry (ICP-AES) revealed 28.3 wt.% Mg (stoichiometric magnesite of composition $MgCO_3$ is expected to have 28.6 wt.%) and trace amounts of elemental impurities (Al, Ca, Fe, K, Na, Sr, Mn). The magnesite specimen was gently grounded and sieved to grain sizes between 354 and 500 μm. The grain surfaces were treated with the same procedure as outlined in Chou et al. (1989). The grains were cleaned with 1% HCl for several seconds and were ultrasonically cleaned in acetone to remove fine particles. The grain were then rinsed with distilled water several times, dried in an oven overnight at 60 °C, and stored in a desiccator. The surface area was determined by N_2 gas sorption using the Brunauer–Emmett–Teller (BET) method (Micromeritics ASAP-2020 surface analyzer). The average BET surface area was measured to be 1.87 m^2/g with a standard deviation of 0.54 m^2/g for three samples. This value may have been high since reported BET surface area values for grounded natural magnesite vary between 0.0662 (Pokrovsky et al., 2005) to 0.224 m^2/g (Pokrovsky et al., 2009; Saldi et al., 2012). On the other hand, BET surface area measured for outcrop chalk cores from carbonate reservoirs have been reported to be around 2.0 m^2/g, similar to those measured in this work (Zhang et al., 2006; Shariatpanahi et al., 2011; Austad et al., 2012). Natural crystalline quartz sand of grain sizes between 354 and 500 μm (Unimin Corporation) was prepared by the same cleaning procedure except that the treatment with HCl was omitted.

3.1.2. Mineral spatial distribution

Two columns with different spatial distributions of magnesite were used in this study, as shown in Fig. 1. The total amount of magnesite is 10% of the overall solid volume in both columns. In the Mixed column, the packing consists of

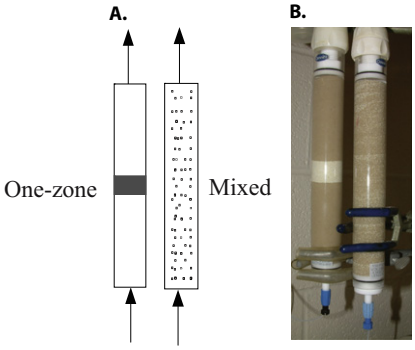

Fig. 1. (A) Schematic representation of the two columns packed with different spatial configuration of magnesite (gray) and quartz (white). (B) Photographs of the 22 cm One-zone and Mixed columns. The volume fraction of magnesite is 10% in both columns. The two columns have the same total BET and geometric surface area for magnesite. In the Mixed column, the packing consists of a random, uniform mixture of magnesite and quartz. In the One-zone column, magnesite grains were distributed as one large zone embedded within a matrix of non-reactive quartz.

a random, uniform mixture of magnesite and quartz, which presumably leads to the highest interphase contact area. In the One-zone column, magnesite grains were distributed as one zone embedded within a matrix of non-reactive quartz. This represents the extreme case where all reactive minerals are clustered and the surface area of the "reactive zone" is small even though the magnesite–water interfacial area is identical compared to the Mixed column. For the One-zone column, the amount of magnesite per unit length in the reactive zone is 10 times higher than that in the homogeneous Mixed case even though both columns have identical overall concentrations of magnesite.

3.1.3. Column packing

Experiments were run with 2.5-cm diameter glass chromatography columns (Omnifit) of varying length (22, 10, and 5 cm). The columns consist of two fixed end caps and a 20 μm polytetrafluoroethylene (PTFE) frit to hold the porous media in place. Columns were "wet packed" (Minyard and Burgos, 2007). In the Mixed column, magnesite and quartz grains were mixed and divided into 22 portions. Initial solution was poured slowly into the column to fill the space in an upward manner to establish a column height of 1 cm. After that, each portion of the solid material was added incrementally until the column was filled. In the case of the One-zone column, the material was weighed and divided into approximately one gram portions. The first half portion of sand was packed into the column with the same packing procedure as described for the Mixed column. Small portions of magnesite were then added incrementally on top of the sand layer until the section between 10 and 11 cm of the column was filled. The other half of quartz was then added on top of the magnesite layer until the column was filled. During packing, columns were tapped on four sides to remove air bubbles and to settle the layers to ensure uniformity. After completion, the columns were secured with the end-cap and connected to a syringe pump (Harvard Apparatus MA1 55–5920). Total pore volume was determined by weighing the column dry and fully saturated. Porosity was determined by dividing the pore volume by the entire volume of each column. The average porosity was measured to be approximately 0.35 with a standard deviation of 0.01.

3.1.4. Flow-through experiments

The experiments were operated at room temperature (~22 °C), with the influent solution flowing upward. The inlet solution contained 10^{-3} M NaCl in deionized water with pH adjusted with HNO_3 to 4. Potassium bromide at a concentration of 10^{-4} M was added as a non-reactive tracer for measurement of dispersivity. The inlet reservoir solution was in equilibrium with the partial pressure of CO_2 in the atmosphere. Effluent samples were collected for 10 residence times. All collected effluent samples were filtered through 0.22 μm filters and acidified with one drop of 2% HNO_3 to prevent precipitation. Effluent samples were analyzed for Mg(II) concentration using a Perkin-Elmer Optima 5300DV inductively coupled plasma-atomic emission spectrometer (ICP-AES). For all column lengths (22, 10, and 5 cm), a series of typical groundwater flow velocities ranging from 0.18 to 36 m/d were used (Newell et al., 1990), covering more than two orders of magnitude.

3.2. Reactive transport modeling

3.2.1. Reactions and species

In the column experiments, in addition to the magnesite dissolution as the kinetically controlled reaction, other aqueous speciation reactions also occur. These aqueous speciation reactions occur instantaneously in comparison to mineral dissolution. The species involved include Mg^{2+}, $MgHCO_3^-$, $MgCO_3$(aq), $H_2CO_3^0$, HCO_3^-, CO_3^{2-}, H^+, OH^-, Na^+, K^+, Cl^-, and Br^-. In a system where both fast and slow reactions occur, the reactive transport formulation partitions the species into primary and secondary species, where the secondary species are written in terms of primary species using the mass action law of the fast reactions (Lichtner, 1985, 1996). In this work, Mg^{2+}, HCO_3^-, H^+, Na^+, K^+, Br^-, Cl^-, and SiO_2(aq) were used as primary species. All other species were considered as secondary species. All reactions and their thermodynamic and kinetic parameters are shown in Table 1. The reaction equilibrium constants for all aqueous speciation reactions are from EQ3/6 database except that of magnesite, as will be discussed later (Wolery et al., 1990). Specifically, the reaction parameters for the magnesite dissolution were obtained by matching the experimental data.

3.2.2. Reactive transport equations

The governing mass conservation equations for the reactive transport system were written for the total concentrations of primary species. As an example, the reactive transport equation for the total concentration of primary species Mg(II) is the following:

$$V\frac{\partial(\phi C_{\mathrm{Mg(II)}})}{\partial t} = V\nabla\cdot(\phi D_{\mathrm{Mg(II)}}\nabla C_{\mathrm{Mg(II)}}) - V\nabla\cdot(\phi v C_{\mathrm{Mg(II)}}) + r_{\mathrm{MgCO_3}}A \quad (5)$$

Table 1
Chemical and physical parameters used in the model.

Chemical parameters	Log K_{eq}	k (mol/m^2/s, this work)	SSA (m^2/g, BET surface area, this work)	k (mol/m^2/s, Chou et al., 1989)	SSA* (m^2/g, geometric surface area, Chou et al., 1989)
Aqueous speciation (at equilibrium)					
$H_2O \Longleftrightarrow H^+ + OH^-$	−14.00	–		–	
$H_2CO_3^0 \Longleftrightarrow H^+ + HCO_3^-$	−6.35	–		–	
$HCO_3^- \Longleftrightarrow H^+ + CO_3^{2-}$	−10.33	–		–	
$MgHCO_3^- \Longleftrightarrow Mg^{2+} + HCO_3^-$	−1.04	–		–	
$MgCO_3(aq) \Longleftrightarrow Mg^{2+} + CO_3^{2-}$	−2.98	–		–	
Kinetic reactions (log K value is log K_{sp} value)					
$MgCO_3(s) + H^+ \rightleftharpoons Mg^{2+} + HCO_3^-$	–	6.20E−5	1.87	2.50E−5	0.025
$MgCO_3(s) + H_2CO_3^0 \rightleftharpoons Mg^{2+} + 2HCO_3^-$	–	5.25E−6	1.87	6.00E−6	0.025
$MgCO_3(s) \rightleftharpoons Mg^{2+}CO_3^{2-}$	−7.83	1.0E−10	1.87	4.50E−10	0.025
Physical parameters					
Porosity	0.35 (±0.01)				
Dispersivity	0.001 m				
Flow velocity	0.18 ~36 m/d				

*Estimated from sphere-shaped geometry assuming a mean grain size of 400 μm.

where V is the total volume of the porous media (m^3), ϕ is the porosity, $C_{Mg(II)}$ is the total concentration of aqueous species that contain Mg^{2+} (mol/m^3, i.e., the summation of the concentrations of Mg^{2+}, $MgHCO_3^+$, and $MgCO_3(aq)$), $D_{Mg(II)}$ is the hydrodynamic dispersion coefficient (m^2/s), v is the flow velocity (m/s), and A is the magnesite surface area (m^2). The value of A was calculated using the measured BET specific surface area (m^2/g) and the mineral mass (g). The reaction rate r_{MgCO3} (mol/m^2/s) is described by the reaction rate law as shown in Eq. (4). The mass accumulation rate of total Mg(II) (left-hand side term) depends on the rate of dispersion and diffusion (1st term on the right hand side (rhs) of the equation), rate of mass flow (2nd term on the rhs), and magnesite dissolution and precipitation (3rd term on the rhs). Similar equations were also written for the total concentrations of other primary species as appropriate. Here the porosity and the specific surface area are assumed equal to the measured values of 0.35 and 1.87 m^2/g, respectively. A value of 0.001 m was used for dispersivity after matching the bromide breakthrough curve. The value is consistent with literature values at similar spatial scales (Gelhar et al., 1992).

3.2.3. Numerical simulation

The mass conservation equations were solved using CrunchFlow, a reactive transport code widely used for many different applications in (bio)geochemical processes in subsurface (Steefel, 2007; Steefel and Maher, 2009; Singha et al., 2011; Li et al., 2011a). The computation domain was set up to mimic that of the magnesite–quartz packing patterns. In the Mixed column, the magnesite was distributed everywhere but with only 10% of the material and therefore 10% of the surface area. In the One-zone column, magnesite was distributed only in the middle section that occupies 10% of the column length, however with 100% surface area. The inlet boundary condition and the initial conditions were set the same as those used in the experiments, as shown in Table 2. The initial pH was set equal to 9, higher than the inlet pH of 4, to avoid fastest magnesite dissolution before the start of flow through experiments. The grid block sizes were set equal to 0.1 cm or smaller, depending on the specific conditions of each simulation. Before each simulation, the resolution of different grid block sizes were tested to determine if the size was high enough to consider each grid block as well-mixed. Specifically, a few grid block sizes were tried and the largest grid block size that produced the same results as a higher resolution run was used.

The effluent aqueous concentration data were used as constraints in the model to determine the kinetic rate constants for magnesite dissolution by trial and error (k values in Table 1). In matching the data, the BET surface area was fixed at the measured value of 1.87 m^2/g, while the kinetic rate constants were varied in order to obtain the best fit to the data. As reported in Table 1, our k_1, k_2, and k_3 values are 2.5, 0.88 and 0.22 times the values given in Chou et al. (1989). Various other sets of kinetic parameters were tried however this is the set that best matches the Mg(II) breakthrough data under different flow conditions. In particular, the k_1 value is important under high-flow rate conditions when the entire column experiences relatively low inlet pH at steady state due to the short residence times. Increasing or decreasing the k_1 value cannot reproduce the Mg(II) data for the flow velocities of 36 m/d. The value of k_3 is important in matching Mg(II) data under slow-flow velocity conditions where the system is close to equilibrium and the column experiences high pH at steady state. The match is not very sensitive to the value of k_2 as the system does not have a high concentration of carbon dioxide. In addition, a K_{sp} value of 1.48E−8 (log $K_{sp} = -7.83$) was used for magnesite. This is higher than the K_{sp} value of 6.61E−9 (log $K_{sp} = -8.20$) reported in Chou et al. (1989) by a factor of 2.34. This is also higher than the reported value of 9.55E−9 (log $K_{sp} = -8.02$) calculated from SUPCRT92 (Johnson et al., 1992) and reported in (Morse et al., 2007) by a factor of 1.58. However, this value is very close to the log K_{sp} value of −7.99 (with a standard devia-

Table 2
Initial and boundary concentrations of all species.*

Species	Initial conditions	Boundary inlet conditions
pH	9.0	4.0
CO_2(aq)	1.07E−5 M	1.07E−5 M
Mg^{2+}	Variable (measured)	0.0 M
Na^+	6.78E−3 M	8.96E−4 M
K^+	1.00E−4 M	1.00E−4 M
Cl^-	1.00E−3 M	1.00E−3 M
Br^-	0.0 M	1.00E−4 M
HCO_3^-	5.35E−3 M	5.07E−8 M
CO_3^{2-}	3.30E−4 M	2.68E−14 M
$MgCO_3$(aq)	Variable	0.0 M
$MgHCO_3^+$	Variable	0.0 M
OH^-	1.12E−5 M	1.06E−10 M
SiO_2(aq)	1.00E−5 M	1.00E−5 M

*Values of pH, and total concentrations of Mg^{2+}, Na^+, K^+, Cl^-, Br^-, and SiO_2(aq) were measured. Concentrations of carbonate species were calculated based on their initial equilibrium with atmospheric CO_2(g) and equilibrium constants of aqueous speciation reactions. Concentrations of other species were calculated based on the measured total concentrations and equilibrium constants of aqueous speciation reactions.

tion of 0.15) at 50 °C reported by Benezeth et al., (2011). Without this K_{sp} adjustment, the code underestimates the Mg(II) effluent concentrations under low-flow conditions where the system reaches equilibrium.

In Chou et al. (1989), the surface area was calculated from an assumed geometric shape (spherical) and the average size of the particles. With a grain size of 354–500 μm, assuming a spherical shape and an average diameter of 400 μm (the particle size used here), the geometric specific surface area for spheres was calculated to be 0.025 m^2/g, i.e., 75 times smaller than our measurement of 1.87 m^2/g. Taking into account the difference in both the surface area and the value of k, the products k_1A, k_2A, and k_3A values are higher here than the corresponding Chou values by approximately a factor of 187, 66, and 17. In addition, our K_{sp} value is also larger. Therefore, the magnesite used in this study has a much larger reactivity than that used in Chou et al. (1989), an observation perhaps consistent with the very high measured value for specific surface area. Recent studies on calcite also found that it is challenging to obtain a one-to-one match for mineral precipitation rates because of the different experimental setup and conditions in different laboratories (Noiriel et al., 2012). The discrepancy is likely influenced also by the different samples of magnesite used. However, in general, the rate constants fall in the range of area-normalized rates reported in the literature for magnesite (Pokrovsky and Schott, 1999; Pokrovsky et al., 2005, 2009).

After matching the data, the model-calculated concentrations of all the pertinent species at different times and locations were used to calculate the local-scale dissolution rates as described in the next section.

3.3. Quantification of dissolution rates at different scales

3.3.1. Local in situ dissolution rates

The local in situ dissolution rates $r_{MgCO_3,i}$ for each grid block i were calculated using Eq. (4), except that the local concentrations in each grid block i were used. The local dissolution rates depend on local aqueous chemistry and vary spatially.

3.3.2. Column-scale dissolution rates

The steady-state column-scale reaction rate R_{MgCO_3} (mol/m^2/s) was calculated as follows:

$$R_{MgCO_3} = \frac{Q_T[C_{Mg(II),out} - C_{Mg(II),in}]}{A_T} = \frac{\sum_{i=1}^{n} r_{MgCO_3,i} A_i}{A_T} \quad (6)$$

Here Q_T is the total flow rate (m^3/s) through the column, $C_{Mg(II),out}$ and $C_{Mg(II),in}$ are the concentrations of Mg(II) in the effluent and influent of the column experiment (mol/L), A_T is the total magnesite surface area within the whole column (m^2), $r_{MgCO_3,i}$ is the rate calculated for grid block i and was determined based on Eq. (4), and A_i is the local magnesite surface area (m^2 at grid block i). Because the effluent concentration was used to constrain the model, both modeling output (last term in (6)) and experimental data (second term in (6)) gave the same dissolution rates for each simulation condition. In (6), the first equation is essentially the definition of the column-scale rate and is simply a statement of mass balance for the column. The second equation states that the column-scale dissolution rate is equivalent to the summation of local scale rates in all grid blocks ($r_{MgCO_3,i}A_i$) divided by the total amount of surface area A_T. Essentially, this states that the column-scale rates are the area-averaged local-scale rates. Model results showed that these two ways of calculating column scale rates were equivalent.

3.3.3. Quantification of the effects of mineral distribution

The effect of mineral spatial distribution on column-scale rates is quantified using the relative ratio α as follows:

$$\alpha = \frac{R_{MgCO_3,One\text{-}zone}}{R_{MgCO_3,Mixed}} = \frac{C_{Mg(II),out,One\text{-}zone} - C_{Mg(II),in,One\text{-}zone}}{C_{Mg(II),out,Mixed} - C_{Mg(II),in,Mixed}} = \frac{\frac{1}{A_{T,One\text{-}zone}} \sum_{i=1}^{n} r_{MgCO_3,i} A_{i,One\text{-}zone}}{\frac{1}{A_{T,Mixed}} \sum_{i=1}^{n} r_{MgCO_3,i} A_{i,Mixed}} \quad (7)$$

Here $R_{MgCO_3,One\text{-}zone}$ and $R_{MgCO_3,Mixed}$ are calculated using Eq. (6) for the One-zone and the Mixed columns, respectively. Under the same flow condition, the Q_T and A_T terms in Eq. (7) are the same for both columns and cancel out in the equation. In this work, inlet concentrations of Mg(II) for all column experiments are zero. As such, the difference in the column-scale rates α can be calculated by the difference in the effluent Mg(II) concentrations.

4. RESULTS

4.1. Effects of mineral spatial distribution

To illustrate the effect of magnesite spatial distribution on transport and dissolution, Fig. 2 shows the breakthrough curves of the non-reactive bromide (2A) and magnesium (2B) from the Mixed and One-zone 22 cm columns at the flow velocity of 3.6 m/d. The tracer breakthrough curves from the Mixed and One zone columns almost overlap, indicating very similar physical properties. A dispersivity value of 0.001 m matched both breakthrough curves very well, as shown in Fig. 2A. For the Mg(II) break-

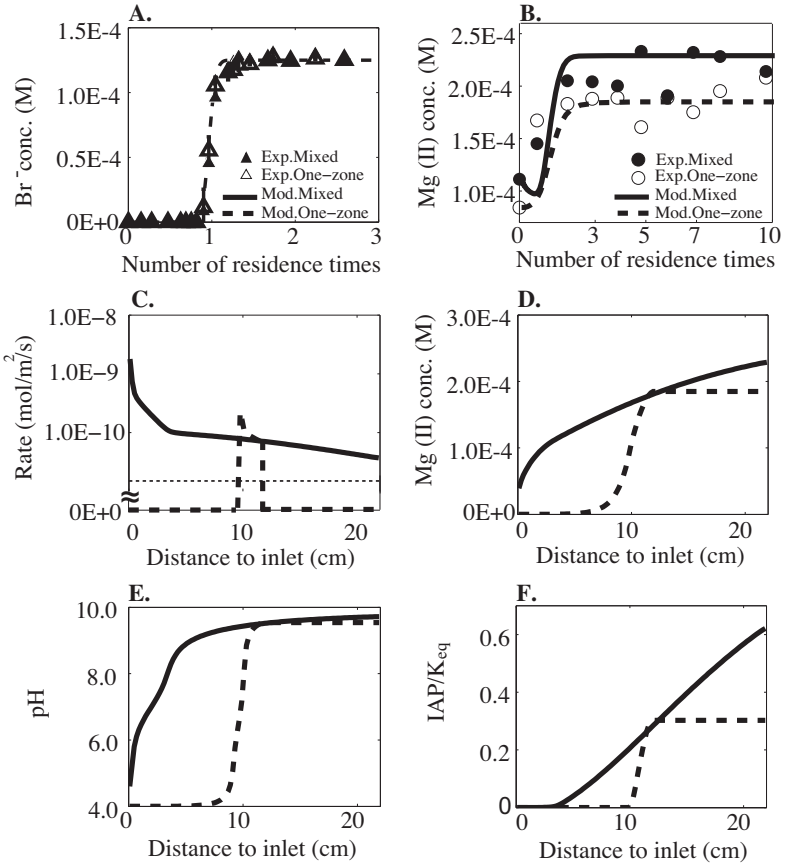

Fig. 2. Experimental data and model predictions for the Mixed and One-zone 22-cm columns under a flow velocity of 3.6 m/d. (A) Experimental tracer breakthrough data (triangles) and modeling output (lines), (B) experimental breakthrough data (dots) and modeling output (lines) of Mg(II); (C to F) predicted spatial distribution of local-scale dissolution rates (C), magnesium concentration (D), pH (E), and IAP/K_{eq} (F).

through, the two columns show similar trends but different rates. The Mg(II) concentrations increased from their initial concentration to their steady state value after about two residence times. At steady state, effluent magnesium concentrations from the Mixed column are higher (approximately 2.17×10^{-4} M) than that from the One-zone column (approximately 1.79×10^{-4} M), indicating a higher column-scale dissolution rate in the Mixed column. Except for some fluctuations, the modeling results reproduced the Mg(II) effluent concentrations in the two columns.

Based on the fit to the effluent Mg concentration, Fig. 2C–F show the model predictions of the steady-state spatial profiles for the local scale dissolution rates, Mg(II), pH, and IAP/K_{eq}. As can be observed in Fig. 2C, the local dissolution rates vary by approximately two orders of magnitude, depending on the local aqueous geochemistry. In the Mixed column, the local dissolution rates are about 10^{-9} mol/m^2/s close to the inlet because of the low pH and far-from-equilibrium conditions as indicated in Fig. 2E and F. In less than 5 cm, pH has increased to values higher than 8 and the rates are orders of magnitude lower than that close to the inlet. Correspondingly, the IAP/K_{eq} values are close to zero for the first several centimeters and increase in the later part of the column gradually.

In the One-zone column, because all magnesite grains are clustered together, magnesite dissolution rates are non-zero only in the middle 10–11 cm. As a result, pH and Mg(II) concentrations are the same as the inlet solution for approximately the first 9 cm of the column. At approximately 10 cm along the column, both dissolution rates and pH increase abruptly due to the presence of magnesite. Values of pH quickly reach ~9.5 at 11 cm, where the magnesite zone ends. This value then remains the same until the end of the column. The IAP/K_{eq} values also show similar patterns. At the end of the columns, the pH values of the two columns are similar. However, the Mixed column has a higher IAP/K_{eq} value, indicating more dissolution of magnesite has brought the outlet fluid closer to equilibrium at the end of the column. This is consistent with the higher effluent magnesium concentration as shown in Fig. 2B.

4.2. Effects of flow velocity

Fig. 3A shows the effect of flow velocity (0.36, 3.6, and 36 m/d) on the effluent magnesium breakthrough in the Mixed and One-zone 22 cm columns. Effluent concentrations all start approximately at 1.0×10^{-4} M at time zero and reach different values under steady state conditions.

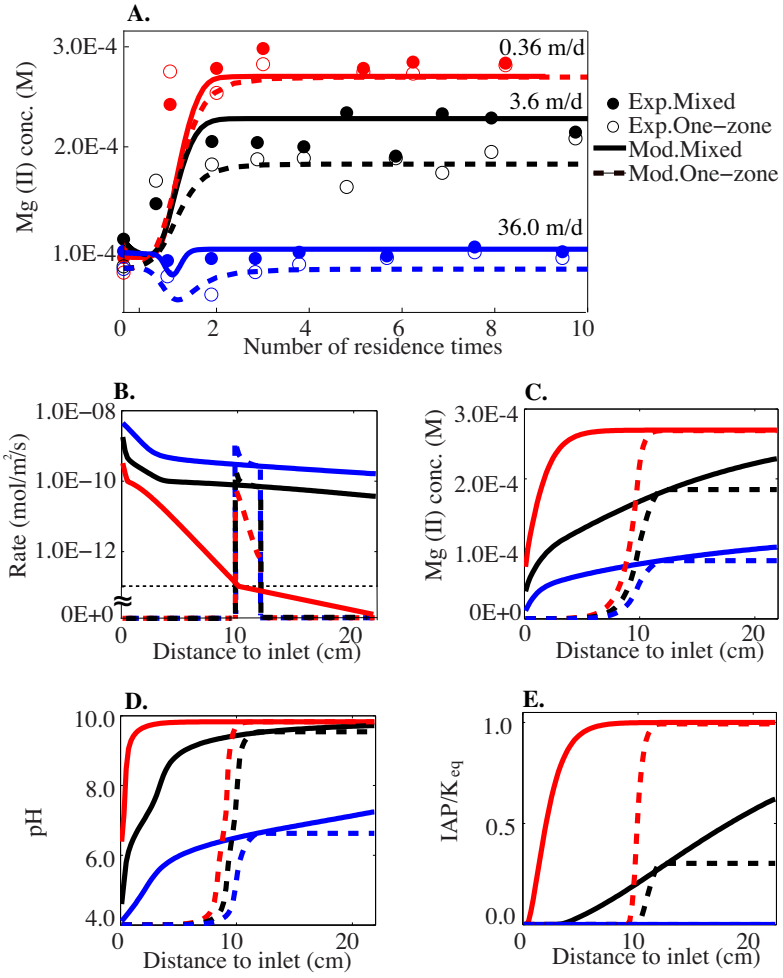

Fig. 3. (A) Experimental data (dots) and modeling output (lines) for magnesium breakthrough curves for the Mixed and One-zone 22 cm columns at three flow velocities (0.36, 3.6, and 36 m/d). Simulated spatial profiles of (B) local dissolution rates, (C) steady state Mg(II) concentration, (D) pH, and (E) IAP/K_{eq} under three different flow velocity conditions. Color scheme is the same for all figures.

In general, the lower the flow velocity, the longer the residence time, and the higher the effluent magnesium concentration at steady state. In both low-flow velocity (0.36 m/d) and high-flow velocity (36 m/d) experiments, the effluent magnesium concentrations are similar for the two columns. At the medium flow velocity of 3.6 m/d, in contrast, the steady state effluent concentrations differ by approximately 14%. The modeling captured the trend of the observed changes. The early dip in the curve during the transient stage is due to the fact that initially there is some Mg(II) dissolved in the column before the flow through experiments. This concentration is higher than the concentration in the inlet fluid at the starting point of the flow-through experiment. This is particularly evident with the flow velocity of 36 m/d due to the short residence time. The model fits the data under steady state conditions, reproducing the magnitude of the difference between the two columns as observed experimentally.

To understand the difference, Fig. 3B–E show the predicted spatial profiles for the two columns. Experimentally imposed variations in hydrodynamic conditions have a significant effect on the concentration fields. At the flow velocity of 0.36 m/d, the reaction products remain in the column for a relatively long period due to the longer residence time. As a result, local dissolution rates are non-zero only in the first couple of centimeters of the column, as shown in Fig. 3B. In effect, pore fluid approaches local chemical equilibrium in most of the column because of the relatively slow flow velocity compared to reaction rate (Knapp, 1989). As a result, the effluent magnesium concentrations at steady state are the same as the equilibrium concentration, as indicated by values of IAP/K_{eq} that are close to unity at the outlet of the column (Fig. 3E).

In the high flow velocity of 36 m/d, however, the fast mass transport moves the reaction products quickly out of the column. As a result, pH remains low, and IAP/K_{eq} is almost zero as shown in Fig. 3E, indicating far-from-equilibrium conditions. The systems operate in a kinetic rather than a local equilibrium regime (Knapp, 1989). Although the local dissolution rate depends on pH, the resulting difference in rates between the two columns is relatively small because they experience very similar pH ranges. In contrast, in the medium flow velocity (3.6 m/d) experiment, the magnitude of the characteristic time scales

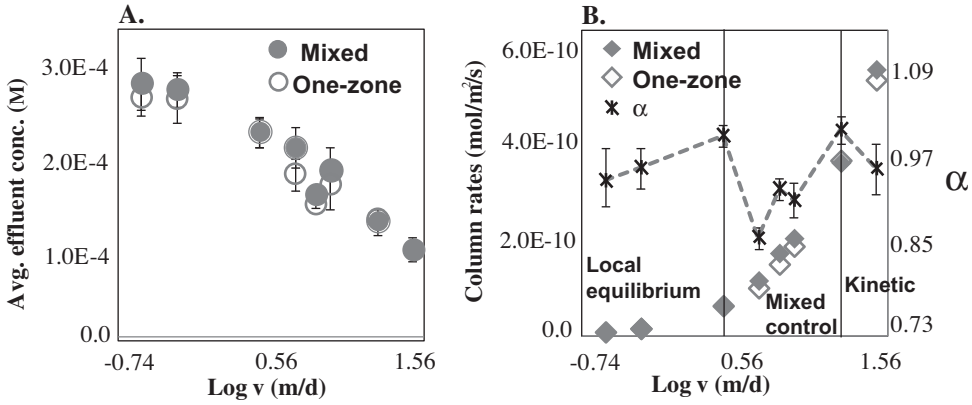

Fig. 4. (A) Average effluent Mg(II) concentrations as a function of the logarithm of flow velocity (v) in the Mixed (●) and One-zone (○) columns (22 cm); (B) column-scale rates for the Mixed (♦) and One-zone (◇) columns and the ratio of the rates from the two columns (α, × and the dashed line). Error bars are indicated for α. The discrepancies between Mixed and One-zone columns are everywhere small but are most pronounced in the experiments with mid-range velocities, i.e., the mixed regime experiment.

for advection and reaction processes are comparable, resulting in a mixed control regime. In the early part of the column, the dissolution is controlled by the pH-dependent reaction kinetics while in the latter part of the column, the reaction is closer to equilibrium and is controlled by the IAP/K_{eq} term. Therefore, the overall dissolution rates in the whole column depend on aqueous geochemistry, which lead to a larger difference between the Mixed and One-zone columns than in the other two flow regimes.

To illustrate the differences between the dissolution rates under all flow velocity conditions, Fig. 4A shows averaged effluent magnesium concentrations from the two 22 cm columns as a function of flow velocity varying from 0.18 to 36 m/d. Each pair of Mg(II) concentrations represents the two column experiments under one flow velocity condition. The average effluent magnesium concentrations under each flow condition were obtained by averaging four effluent magnesium concentrations at steady state. The error bar represents the standard deviation of the measured data. Effluent magnesium concentrations for both columns decreased with increasing flow velocity. This is consistent with the observations in Fig. 3.

Fig. 4B shows column-scale rates under different flow velocity conditions. In general, the column-scale rate increases with increasing flow velocity, although the effluent concentration decreases. This is because the dissolution rate is the product of effluent concentration and flow rate, as shown in Eq. (6). At high flow velocity, although the effluent concentration is low, the flow rate is much higher. This is consistent with the relatively low pH values, far-from-equilibrium conditions, and higher local-scale dissolution rates under high flow velocity conditions, as shown in Fig. 3.

The ratio of the column-scale rates between the two columns (α, as defined in Eq. (7)) and its error bar are shown as a function of flow velocity in Fig. 4B. The ratio is close to one for low flow velocities of 0.18 and 0.36 m/d, where the flow is in the local equilibrium regime. The ratio is also close to one at high flow velocities of 18.0 and 36.0 m/d, where the flow is in the kinetic regime. It is at the medium flow velocity of 3.6 m/d that the ratio reaches its minimum value of 0.86, the largest difference between the two columns (i.e., 14%, the mixed control regime).

4.3. Effects of length scale

To understand the effects of column length on rates at different spatial scales, Fig. 5A shows the predicted distribution of local rates (lines) and their corresponding column-scale rates (diamonds) in six columns (Mixed and One-zone columns at 5, 10, and 22 cm). For the Mixed columns, the curves for the local-scale rates in the 5 cm and 10 columns overlap with those in the first 5 cm and 10 cm of the 22 cm columns, respectively. This is an obvious result indicating that the shorter columns represent the early part a subsection of the longer column. For the One-zone columns, the local-scale rates are non-zero in distinct middle zones where magnesite is present.

The column-scale rates for the 5 cm and 10 cm columns represent the integrated rates over the first 5 and 10 cm of the 22 columns, respectively. The 5 cm column has the highest column-scale rates while the 22 cm column has the lowest column-scale rates. This can be explained by the relatively lower pH, IAP/K_{eq} values, and higher local rates in the shorter columns, as can be observed from Fig. 5A, C, and D. The lower pH and IAP/K_{eq} values lead to higher local rates, which collectively lead to higher column scale rates in the 5 cm column than in longer columns.

4.4. Combined effects of all three factors

Fig. 6 shows the effluent concentrations, the column-scale dissolution rates, and the difference between the two columns under all experimental conditions. In general, similar trends were observed as explained in previous sections. Fig. 6A shows that the effluent magnesium concentrations decrease with increasing flow velocity and decreasing column length. Fig. 6B shows that column-scale rates increase with increasing flow velocity and decreasing column length. Fig. 6B also shows α values under all conditions. The figure indicates that the mineral spatial distribution plays a role in determining the dissolution rates under medium-flow con-

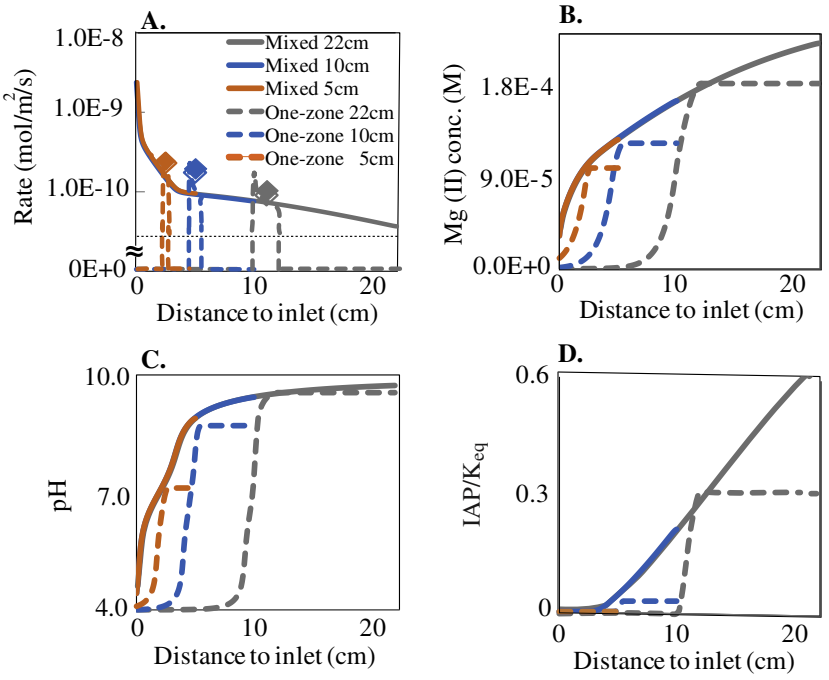

Fig. 5. Predicted spatial profiles of (A) rates, (B) aqueous Mg(II), (C) pH, and (D) IAP/K_{eq} for column lengths of 5 (orange lines), 10 (blue lines), and 22 cm (gray lines) at the flow velocity of 3.6 m/d. The diamonds in (A) are the column-scale rates for the six columns. (For interpretation of the references to colour in this figure legend, the reader is referred to the web version of this article.)

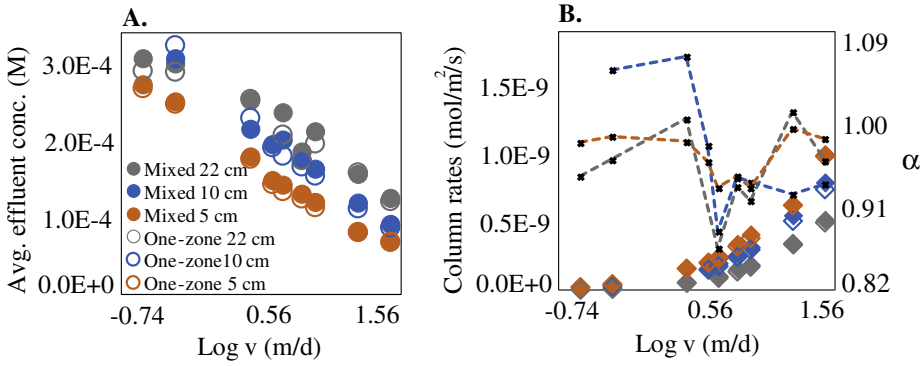

Fig. 6. (A) Effluent Mg(II) concentrations, (B) column-scale dissolution rates (left y axis, diamonds), and difference between the two columns (right y axis, α, ×-symbols and dashed lines) under all flow velocity, column length, and mineral distribution conditions. Color schemes are the same as in other figures.

ditions, although the differences for this mineral and set of conditions are not significant. The largest difference was observed at a medium-flow velocity of 3.6 m/d for all three column lengths. The extent of difference reaches a maximum with the 22 cm column.

To understand the controlling parameters that affect the column-scale dissolution rates, we define the dimensionless Damkohler number Da_I at the column scale that that quantifies the relative dominance of advection and dissolution in the systems:

$$Da_I = \frac{\tau_{adv}}{\tau_r} = \frac{\frac{L}{v}}{\frac{V_p C_{eq,Mg}}{R_{MgCO_3} A_T}} = \frac{L R_{MgCO_3} A_T}{v V_p C_{eq,Mg}} \quad (8)$$

This number compares the relative significance of reaction and advection at the column scale. The characteristic time scale for advection is the residence time of fluid in the column, defined as $\tau_{adv} = \frac{L}{v}$, where L is the length of the column (m) and v is the average flow velocity (m/d). The characteristic time scale for dissolution is essentially the time that it takes to reach equilibrium in the entire column. This is defined as $\tau_r = \frac{V_p C_{eq,Mg}}{R_{MgCO_3} A_T}$, where V_p is the total pore volume of the column (m^3), $C_{eq,Mg}$ is the equilibrium concentration of Mg(II) (mol/m^3), R_{MgCO_3} is the column-scale dissolution rate ($mol/m^2/s$), and A_T is the total surface area in the column (m^2).

The logarithms of the column-scale rates under all conditions as a function of Da_I are shown in Fig. 7. The figure shows that Da_I is a good indicator of the dissolution rates under different conditions. This is consistent with the conclusion that the column-scale dissolution rates are controlled by the relative rates of reaction versus advection.

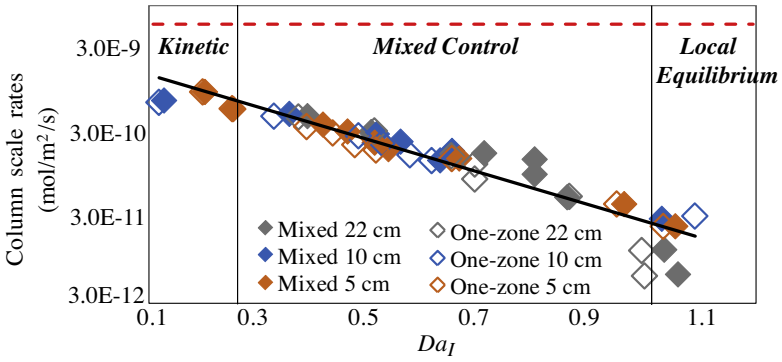

Fig. 7. Column-scale rates plotted as a function of Da_I. The data shows that Da_I is a good predictor of the column-scale dissolution rates. The red dashed line represents the rates calculated under well-mixed conditions at a pH of 4 (prediction based on Eq. (4)).

The column-scale dissolution rates decrease with increasing Da_I values, which means that the lower the flow velocities or the longer the column lengths, the lower the column-scale dissolution rates. High Da_I values indicate long residence time (low flow velocity or long column length) relative to the time to reach equilibrium and are consistent with a local equilibrium regime. Across all the experiments, the rates depend largely on the relative rates of advection and dissolution. In addition, rates are orders of magnitude lower, and are very sensitive to Da_I, especially when this ratio is larger than 0.95. In contrast, low Da_I values are consistent with high flow velocity, high dissolution rates, and the kinetic flow regime. In this flow regime, the dissolution rate is essentially determined by the intrinsic kinetics of magnesite dissolution and therefore does not change significantly with Da_I. As a result, the logarithms of the rates are almost horizontal on the figure. In the mixed flow regime, the logarithms of the rates show a linear dependence on the values of Da_I and can be quantitatively described as follows:

$$\log R_{MgCO_3} = -1.9Da_I - 8.6 \quad (9)$$

Here R_{MgCO_3} is column-scale rate in the units of mol m^{-2} s^{-1}, and Da_I is defined as in Eq. (9). This equation was obtained by regression, yielding a coefficient of determination (R^2) equal to 0.895. Fig. 7 shows that under conditions of $0.3 < Da_I < 0.95$, some differences between the Mixed and the One-zone cases are observed.

For the experimental conditions overall, the column-scale dissolution rates vary from about 6.40×10^{-12} to 1.02×10^{-9} mol m^{-2} s^{-1}, covering approximately two and a half orders of magnitude. The dissolution rate at pH 4 under well-mixed conditions using the k values from this work was calculated and plotted on the figure as well (approximately 6.47×10^{-9} mol m^{-2} s^{-1}). This value is approximately one to three orders of magnitude higher than the observed column-scale dissolution rates. The figure also shows that with small Da_I value, the column-scale rates are closer to the rates calculated for a well-mixed reactor with magnesite dissolving at inlet pH 4.

5. DISCUSSION AND CONCLUSIONS

In this work, we found that column-scale rates measured under different conditions vary between 6.40×10^{-12} and 1.02×10^{-9} mol/m^2/s, approximately 1–3 orders of magnitude slower than those measured in well-mixed reactors directly at the inlet pH of 4 (Fig. 7). Under any particular set of conditions, local in situ dissolution rates vary by orders of magnitude over a length scale of a few to a couple of ten centimeters, depending on local aqueous geochemistry. Column-scale rates depend on several factors that influence the distribution of local dissolution rates. Of the variables tested, the largest impact on column-scale dissolution rates was flow velocity. A two order of magnitude difference in flow velocity was observed to cause more than a two order of magnitude difference in column-scale rates. The column-scale dissolution rates also depend on the spatial scales. With other conditions remaining the same, the column-scale rates are higher with the relatively short columns and they decrease with increasing column length. This could have interesting applications in interpreting field data. Essentially, this is a statement that if the "observation window" for dissolution changes, the observed rates will change as well. In fact, dissolution rates are known to change with the observation window in laboratory and field measurements (Navarre-Sitchler and Brantley, 2007).

The importance of flow velocity and length scale (or fluid residence time) has been discussed before by many others with respect to natural geochemical rates (Knapp, 1989; Schnoor, 1990; Steefel et al., 2005; Maher, 2010). Our results systematically quantified the rates of magnesite dissolution with different fluid residence time using well-controlled experiments and reactive transport modeling. In addition, this work shows that differences in mineral spatial distribution cause a relatively small difference (maximum of 14%). The greatest discrepancy was observed in experiments with medium flow velocities where the systems are under mixed control instead of the local equilibrium or kinetic regimes. Although low and high flow velocity conditions are characterized as operating within the two different regimes – local equilibrium and kinetic – they both showed little difference between the Mixed and One-zone columns. In contrast, experiments with the medium flow velocity, 3.6 m/d (the mixed regime), showed the largest difference between the Mixed and One-zone columns. Under low flow velocity conditions, due to the long residence time, the system reaches local equilibrium and maintains a relatively uniform distribution of aqueous geochemistry and local

dissolution rates. In the high flow velocity (kinetic regime), transport is not limiting and the system becomes surface reaction (interface or kinetic) controlled. As a result, the distribution of aqueous geochemistry is again relatively uniform and the local dissolution rates cover a relatively small range. Under the medium flow regime where the system is under mixed control, the column experiences a larger spatial variation in aqueous geochemistry and in local dissolution rates. As a result, chemical heterogeneity affects the column-scale dissolution rates to a measurable extent.

Column-scale rate data were best understood in terms of the Damkohler number that quantifies the relative dominance of advection and dissolution processes. This dimensionless number should be useful in understanding why field rates tend to be slower than laboratory rates (White and Brantley, 2003) and all field studies should summarize the estimated values of this number. Furthermore, the observations in this study lead us to surmise that rates of weathering may be affected by chemical heterogeneity in natural systems for conditions where both reaction rate and flow rate are similar – i.e., where $0.3 < Da_I < 0.95$. Few if any estimates of the Damkohler number are presented in the literature for field weathering studies (Li et al., 2008; Lebedeva et al., 2010; Brantley and Lebedeva, 2011).

Although the effects of mineral distribution explored in this study are relatively small (maximum of 14%), this does not mean heterogeneity is in general unimportant in natural systems. Here we focus on the layered distribution with the main flow direction perpendicular to the layers, which does not allow for fluid flow to bypass the layers. As such, this case represents scenarios similar to chemical weathering conditions where water flows down into porous horizontally-layered media to form soils. In effect this work represents the scenario that would lead to the lowest impacts of chemical heterogeneity. However, many soils (and other dissolving porous rock systems) also have heterogeneities that are aligned along flow lines. For example, the flow can be parallel to the layered mineral structure and some layers can have lower permeability than others by orders of magnitude (Gelhar and Axness, 1983; Tompson and Gelhar, 1990; Rajaram and Gelhar, 1995; de Marsily et al., 2005). In these scenarios, we expect that the effects of chemical heterogeneity can be considerably larger due to the large extent of transport limitation exerted by the permeability contrast. The fact that the flow velocity can lead to orders of magnitude difference in column-scale dissolution rates indicates that the coupled chemical and physical heterogeneities can significantly affect mineral dissolution rates in natural subsurface.

By quantifying the dissolution rates in well-controlled column experiments under a series of flow velocity, length scale, and mineral spatial distribution conditions, this paper helps explain the observations of laboratory-field rate discrepancies because natural systems experience various flow and mineral distribution conditions at different length scales. In field studies, weathering rates are typically inferred from profiles of mineral concentrations or effluent concentrations at different depth or position along flow paths (Brantley and White, 2009). Typically, detailed concentrations at different positions or different times are largely unknown and it is challenging to quantify the contribution of different factors. For example, one of the ways to calculate dissolution rate in the field is to look at solute chemistry versus depth or lateral position (i.e., position along a flow line). The slope of solute concentration versus depth or position can be used to infer the dissolution rate (Murphy et al., 1998; White, 2002). Fig. 5B exemplifies this technique. However, there is significant difference between the curves for the Mixed column and those from the One-zone column. The dissolution rates inferred from the solute profile of the Mixed column therefore can significantly differ from that using the One-zone profile, although the actual column-scale rates only differ by a maximum of 14%. Importantly, in most field systems, when we sample pore water we typically only get a few samples so we do not see the whole profile. If only two or three samples are obtained, the calculated rates will generally be different for the One-zone and the Mixed systems. Future efforts to and measure and understand how the mineral distribution affects the interpretation of field-scale rates will elucidate why laboratory and field measurements are often different.

ACKNOWLEDGMENTS

This work is supported by start-up funds for Li Li through the Penn State Institutes of Energy and the Environment (PSIEE), the Penn State Laboratory for Isotopes and Minerals in the Environment, and the Penn State Earth and Environmental Systems Institute. S.L.B. cites support from DOE Office of Basic Energy Sciences DE FG02 05ER15675. We acknowledge two anonymous reviewers for their careful and insightful comments that have significantly improved the paper.

REFERENCES

Alekseyev V. A., Medvedeva L. S., Prisyagina N. I., Meshalkin S. S. and Balabin A. I. (1997) Change in the dissolution rates of alkali feldspars as a result of secondary mineral precipitation and approach to equilibrium. *Geochim. Cosmochim. Acta* **61**, 1125–1142.

Anbeek C. (1993) The effect of natural weathering on dissolution rates. *Geochim. Cosmochim. Acta* **57**, 4963–4975.

Anderson S. P., Dietrich W. E. and Brimhall G. H. (2002) Weathering profiles, mass-balance analysis, and rates of solute loss: linkages between weathering and erosion in a small, steep catchment. *Geol. Soc. Am. Bull.* **114**, 1143–1158.

Austad T., Shariatpanahi S. F., Strand S., Black C. J. J. and Webb K. J. (2012) Conditions for a low-salinity enhanced oil recovery (EOR) effect in carbonate oil reservoirs. *Energy Fuels* **26**, 569–575.

Bain J. G., Mayer K. U., Blowes D. W., Frind E. O., Molson J. W. H., Kahnt R. and Jenk U. (2001) Modelling the closure-related geochemical evolution of groundwater at a former uranium mine. *J. Contam. Hydrol.* **52**, 109–135.

Benezeth P., Saldi G. D., Dandurand J.-L. and Schott J. (2011) Experimental determination of the solubility product of magnesite at 50 to 200 °C. *Chem. Geol.* **286**, 21–31.

Berkowitz B. (2002) Characterizing flow and transport in fractured geological media: a review. *Adv. Water Resour.* **25**, 861–884.

Berner R. A. (1978) Rate control of mineral dissolution under earth surface conditions. *Am. J. Sci.* **278**, 1235–1252.

Brantley S. L. (2010) Weathering rock to regolith. *Nat. Geosci.* **3**, 305–306.

Brantley S. L., Bandstra J., Moore J. and White A. F. (2008) Modelling chemical depletion profiles in regolith. *Geoderma* **145**, 494–504.

Brantley S. L. and Lebedeva M. (2011) Learning to read the chemistry of regolith to understand the critical zone. In *Annual Review of Earth and Planetary Sciences* (eds. R. Jeanloz and K. H. Freeman), vol. **39**.

Brantley S. L. and White A. F. (2009) Approaches to modeling weathered regolith. *Thermodyn. Kinet. Water–Rock Interact.* **70**, 435–484.

Brimhall G. H. and Dietrich W. E. (1987) Constitutive mass balance relations between chemical-composition, volume, density, porosity, and strain in metasomatic hydrochemical systems – results on weathering and pedogenesis. *Geochim. Cosmochim. Acta* **51**, 567–587.

Casey W. H. (1987) Heterogeneous kinetics and diffusion boundary-layers – the example of reaction in a fracture. *J. Geophys. Res. – Solid Earth Planets* **92**, 8007–8013.

Casey W. H., Banfield J. F., Westrich H. R. and McLaughlin L. (1993) What do dissolution experiments tell us about natural weathering? *Chem. Geol.* **105**, 1–15.

Castro-Alcala E., Fernandez-Garcia D., Carrera J. and Bolster D. (2012) Visualization of mixing processes in a heterogeneous sand box aquifer. *Environ. Sci. Technol.* **46**, 3228–3235.

Chang H.-s., Um W., Rod K., Serne R. J., Thompson A., Perdrial N., Steefel C. I. and Chorover J. (2011) Strontium and cesium release mechanisms during unsaturated flow through waste-weathered Hanford sediments. *Environ. Sci. Technol.* **45**, 8313–8320.

Chen J. S., Hubbard S. and Rubin Y. (2001) Estimating the hydraulic conductivity at the South Oyster Site from geophysical tomographic data using Bayesian techniques based on the normal linear regression model. *Water Resour. Res.* **37**, 1603–1613.

Chen J. S., Hubbard S. S., Williams K. H., Pride S., Li L., Steefel C. and Slater L. (2009) A state-space Bayesian framework for estimating biogeochemical transformations using time-lapse geophysical data. *Water Resour. Res.* **45**.

Chou L., Garrels R. M. and Wollast R. (1989) Comparative study of the kinetics and mechanisms of dissolution of carbonate minerals. *Chem. Geol.* **78**, 269–282.

Chris A. (1993) The effect of natural weathering on dissolution rates. *Geochim. Cosmochim. Acta* **57**, 4963–4975.

Cirpka O. A., Schwede R. L., Luo J. and Dentz M. (2008) Concentration statistics for mixing-controlled reactive transport in random heterogeneous media. *J. Contam. Hydrol.* **98**, 61–74.

Cirpka O. A. and Valocchi A. J. (2007) Two-dimensional concentration distribution for mixing-controlled bioreactive transport in steady state. *Adv. Water Resour.* **30**, 1668–1679.

Dagan G. (1990) Transport in heterogeneous porous formations – spatial moments, ergodicity, and effective dispersion. *Water Resour. Res.* **26**, 1281–1290.

de Marsily G., Delay F., Goncalves J., Renard P., Teles V. and Violette S. (2005) Dealing with spatial heterogeneity. *Hydrogeol. J.* **13**, 161–183.

Dentz M., Cortis A., Scher H. and Berkowitz B. (2004) Time behavior of solute transport in heterogeneous media: transition from anomalous to normal transport. *Adv. Water Resour.* **27**, 155–173.

Dentz M., Gouze P. and Carrera J. (2011a) Effective non-local reaction kinetics for transport in physically and chemically heterogeneous media. *J. Contam. Hydrol.* **120–21**, 222–236.

Dentz M., Le Borgne T., Englert A. and Bijeljic B. (2011b) Mixing, spreading and reaction in heterogeneous media: a brief review. *J. Contam. Hydrol.* **120–21**, 1–17.

Dibble W. E. and Tiller W. A. (1981) Nonequilibrium water–rock interactions. 1. Model for interface-controlled reactions. *Geochim. Cosmochim. Acta* **45**, 79–92.

Fetter C. W. (1999) *Contaminant Hydrogeology*. Waveland Press, Inc., Long Grove, IL.

Freeze R. A. (1975) A stochastic-conceptual analysis of one-dimensional groundwater flow in nonuniform homogeneous media. *Water Resour. Res.* **11**, 725–741.

Freeze R. A. and Cherry J. A. (1979) *Groundwater*. Prentice Hall, Inc., Upper Saddle River.

Frye E., Bao C., Li L. and Blumsack S. (2012) Environmental controls of cadmium desorption during CO_2 leakage. *Environ. Sci. Technol.* **46**, 4388–4395.

Gautelier M., Oelkers E. H. and Schott J. (1999) An experimental study of dolomite dissolution rates as a function of pH from −0.5 to 5 and temperature from 25 to 80 °C. *Chem. Geol.* **157**, 13–26.

Gelhar L. W. (1993) *Stochastic Subsurface Hydrology*. Prentice-Hall, Englewood Cliffs, NJ.

Gelhar L. W. and Axness C. L. (1983) Three-dimensional stochastic analysis of macrodispersion in aquifers. *Water Resour. Res.* **19**, 161–180.

Gelhar L. W., Welty C. and Rehfeldt K. R. (1992) A critical-review of data on field-scale dispersion in aquifers. *Water Resour. Res.* **28**, 1955–1974.

Glassley W. E., Simmons A. M. and Kercher J. R. (2002) Mineralogical heterogeneity in fractured, porous media and its representation in reactive transport models. *Appl. Geochem.* **17**, 699–708.

Hodson M. E. (2003) The influence of Fe-rich coatings on the dissolution of anorthite at pH 2.6. *Geochim. Cosmochim. Acta* **67**, 3355–3363.

Hubbard S. S. and Rubin Y. (2000) Hydrogeological parameter estimation using geophysical data: a review of selected techniques. *J. Contam. Hydrol.* **45**, 3–34.

Jin L. X., Ravella R., Ketchum B., Bierman P. R., Heaney P., White T. and Brantley S. L. (2010) Mineral weathering and elemental transport during hillslope evolution at the Susquehanna/Shale Hills Critical Zone Observatory. *Geochim. Cosmochim. Acta* **74**, 3669–3691.

Johnson J. W., Oelkers E. H. and Helgeson H. C. (1992) SUPCRT92: a software package for calculating the standard molal thermodynamic properties of minerals, gases, aqueous species, and reactions from 1 to 5000 bar and 0 to 1000 °C. *Comput. Geosci.* **18**, 899–947.

Knapp R. B. (1989) Spatial and temporal scales of local equilibrium in dynamic fluid–rock systems. *Geochim. Cosmochim. Acta* **53**, 1955–1964.

Knutson C., Valocchi A. and Werth C. (2007) Comparison of continuum and pore-scale models of nutrient biodegradation under transverse mixing conditions. *Adv. Water Resour.* **30**, 1421–1431.

Knutson C. E., Werth C. J. and Valocchi A. J. (2005) Pore-scale simulation of biomass growth along the transverse mixing zone of a model two-dimensional porous medium. *Water Resour. Res.* **41**.

Kump L. R., Brantley S. L. and Arthur M. A. (2000) Chemical weathering, atmospheric CO_2, and climate. *Ann. Rev. Earth Planet Sci.* **28**, 611–667.

Landrot G., Ajo-Franklin J. B., Yang L., Cabrini S. and Steefel C. I. (2012) Measurement of accessible reactive surface area in a sandstone, with application to CO_2 mineralization. *Chem. Geol.* **318**, 113–125.

Lebedeva M. I., Fletcher R. C., Balashov V. N. and Brantley S. L. (2007) A reactive diffusion model describing transformation of bedrock to saprolite. *Chem. Geol.* **244**, 624–645.

Lebedeva M. I., Fletcher R. C. and Brantley S. L. (2010) A mathematical model for steady-state regolith production at constant erosion rate. *Earth Surf. Proc. Land.* **35**, 508–524.

Li L., Peters C. A. and Celia M. A. (2006) Upscaling geochemical reaction rates using pore-scale network modeling. *Adv. Water Resour.* **29**, 1351–1370.

Li L., Peters C. A. and Celia M. A. (2007a) Applicability of averaged concentrations in determining geochemical reaction rates in heterogeneous porous media. *Am. J. Sci.* **307**, 1146–1166.

Li L., Peters C. A. and Celia M. A. (2007b) Effects of mineral spatial distribution on reaction rates in porous media. *Water Resour. Res.* **43**. http://dx.doi.org/10.1029/2005WR004848.

Li L., Peters C. A. and Celia M. A. (2007c) Reply to "Comment on upscaling geochemical reaction rates using pore-scale network modeling" by Peter C. Lichtner and Qinjun Kang. *Adv. Water Resour.* **30**, 691–695.

Li L., Steefel C. I. and Yang L. (2008) Scale dependence of mineral dissolution rates within single pores and fractures. *Geochim. Cosmochim. Acta* **72**, 360–377.

Li L., Steefel C. I., Kowalsky M. B., Englert A. and Hubbard S. S. (2010) Effects of physical and geochemical heterogeneities on mineral transformation and biomass accumulation during a biostimulation experiment at Rifle, Colorado. *J. Contam. Hydrol.* **112**, 45–63.

Li L., Gawande N., Kowalsky M. B., Steefel C. I. and Hubbard S. S. (2011) Physicochemical heterogeneity controls on uranium bioreduction rates at the field scale. *Environ. Sci. Technol.* **45**, 9959–9966.

Lichtner P. C. (1985) Continuum model for simultaneous chemical-reactions and mass-transport in hydrothermal systems. *Geochim. Cosmochim. Acta* **49**, 779–800.

Lichtner P. C. (1996) Continuum formulation of multicomponent-multiphase reactive transport. In *Reactive Transport in Porous Media* (eds. P. C. Lichtner, C. I. Steefel and E. H. Oelkers). Mineralogical Society of America, Washington, DC.

Luttge A. (2005) Etch pit coalescence, surface area, and overall mineral dissolution rates. *Am. Mineral.* **90**, 1776–1783.

Luttge A. and Arvidson R. S. (2008) The mineral–water interface. In *Kinetics of Water–Rock Interaction* (eds. S. L. Brantley, J. D. Kubicki and A. F. White). Springer.

Luttge A., Bolton E. W. and Lasaga A. C. (1999) An interferometric study of the dissolution kinetics of anorthite: the role of reactive surface area. *Am. J. Sci.* **299**, 652–678.

Maher K. (2010) The dependence of chemical weathering rates on fluid residence time. *Earth Planet. Sci. Lett.* **294**, 101–110.

Maher K. (2011) The role of fluid residence time and topographic scales in determining chemical fluxes from landscapes. *Earth Planet. Sci. Lett.* **312**, 48–58.

Maher K., DePaolo D. J. and Lin J. C. F. (2004) Rates of silicate dissolution in deep-sea sediment: in situ measurement using U-234/U-238 of pore fluids. *Geochim. Cosmochim. Acta* **68**, 4629–4648.

Maher K., Steefel C. I., DePaolo D. J. and Viani B. E. (2006) The mineral dissolution rate conundrum: insights from reactive transport modeling of U isotopes and pore fluid chemistry in marine sediments. *Geochim. Cosmochim. Acta* **70**, 337–363.

Maher K., Steefel C. I., White A. F. and Stonestrom D. A. (2009) The role of reaction affinity and secondary minerals in regulating chemical weathering rates at the Santa Cruz Soil Chronosequence, California. *Geochim. Cosmochim. Acta* **73**, 2804–2831.

Malmstrom M. E., Destouni G., Banwart S. A. and Stromberg B. H. E. (2000) Resolving the scale-dependence of mineral weathering rates. *Environ. Sci. Technol.* **34**, 1375–1378.

Malmstrom M. E., Destouni G. and Martinet P. (2004) Modeling expected solute concentration in randomly heterogeneous flow systems with multicomponent reactions. *Environ. Sci. Technol.* **38**, 2673–2679.

Meile C. and Tuncay K. (2006) Scale dependence of reaction rates in porous media. *Adv. Water Resour.* **29**, 62–71.

Minyard M. L. and Burgos W. D. (2007) Hydrologic flow controls on biologic iron(III) reduction in natural sediments. *Environ. Sci. Technol.* **41**, 1218–1224.

Miralles-Wilhelm F. and Gelhar L. W. (2000) Stochastic analysis of oxygen-limited biodegradation in heterogeneous aquifers with transient microbial dynamics. *J. Contam. Hydrol.* **42**, 69–97.

Molins S., Trebotich D., Steefel C. I. and Shen C. (2012) An investigation of the effect of pore scale flow on average geochemical reaction rates using direct numerical simulation. *Water Resour. Res.* **48**.

Moore J., Lichtner P. C., White A. F. and Brantley S. L. (2012) Using a reactive transport model to elucidate differences between laboratory and field dissolution rates in regolith. *Geochim. Cosmochim. Acta* **93**, 235–261.

Morse J. W. and Arvidson R. S. (2002) The dissolution kinetics of major sedimentary carbonate minerals. *Earth Sci. Rev.* **58**, 51–84.

Morse J. W., Arvidson R. S. and Luttge A. (2007) Calcium carbonate formation and dissolution. *Chem. Rev.* **107**, 342–381.

Murphy S. F., Brantley S. L., Blum A. E., White A. F. and Dong H. L. (1998) Chemical weathering in a tropical watershed, Luquillo mountains, Puerto Rico: II. Rate and mechanism of biotite weathering. *Geochim. Cosmochim. Acta* **62**, 227–243.

Murphy W. M., Oelkers E. H. and Lichtner P. C. (1989) Surface reaction versus diffusion control of mineral dissolution and growth rates in geochemical processes. *Chem. Geol.* **78**, 357–380.

Navarre-Sitchler A. and Brantley S. (2007) Basalt weathering across scales. *Earth Planet. Sci. Lett.* **261**, 321–334.

Navarre-Sitchler A., Steefel C. I., Yang L., Tomutsa L. and Brantley S. L. (2009) Evolution of porosity and diffusivity associated with chemical weathering of a basalt clast. *J. Geophys. Res. – Earth Surface* **114**.

Newell C. J., Hopkins L. P. and Bedient P. B. (1990) A hydrogeologic database for groundwater modeling. *Ground Water* **28**, 703–714.

Noiriel C., Made B. and Gouze P. (2007) Impact of coating development on the hydraulic and transport properties in argillaceous limestone fracture. *Water Resour. Res.* **43**.

Noiriel C., Steefel C. I., Yang L. and Ajo-Franklin J. (2012) Upscaling calcium carbonate precipitation rates from pore to continuum scale. *Chem. Geol.* **318**, 60–74.

Nugent M. A., Brantley S. L., Pantano C. G. and Maurice P. A. (1998) The influence of natural mineral coatings on feldspar weathering. *Nature* **395**, 588–591.

Peters C. A. (2009) Accessibilities of reactive minerals in consolidated sedimentary rock: an imaging study of three sandstones. *Chem. Geol.* **265**, 198–208.

Plummer L. N. and Wigley T. M. L. (1976) The dissolution of calcite in CO_2-saturated solutions at 25 °C and 1 atmosphere total pressure. *Geochim. Cosmochim. Acta* **40**, 191–202.

Pokrovsky O. S., Golubev S. V. and Schott J. (2005) Dissolution kinetics of calcite, dolomite and magnesite at 25 °C and 0 to 50 atm pCO_2. *Chem. Geol.* **217**, 239–255.

Pokrovsky O. S., Golubev S. V., Schott J. and Castillo A. (2009) Calcite, dolomite and magnesite dissolution kinetics in aqueous

solutions at acid to circumneutral pH, 25 to 150 °C and 1 to 55 atm CO_2: new constraints on CO_2 sequestration in sedimentary basins. *Chem. Geol.* **265**, 20–32.

Pokrovsky O. S. and Schott J. (1999) Processes at the magnesium-bearing carbonates/solution interface. II. Kinetics and mechanism of magnesite dissolution. *Geochim. Cosmochim. Acta* **63**, 881–897.

Rajaram H. and Gelhar L. W. (1995) Plume-scale dependent dispersion in aquifers with a wide-range of scales of heterogeneity. *Water Resour. Res.* **31**, 2469–2482.

Rickard D. and Sjoberg E. L. (1983) Mixed kinetic control of calcite dissolution rates. *Am. J. Sci.* **283**, 815–830.

Rosso J. J. and Rimstidt J. D. (2000) A high resolution study of forsterite dissolution rates. *Geochim. Cosmochim. Acta* **64**, 797–811.

Rubin Y. and Gomez-Hernandez J. J. (1990) A stochastic approach to the problem of upscaling of conductivity in disordered media: theory and unconditional numerical simulations. *Water Resour. Res.* **26**, 691–701.

Saldi G. D., Jordan G., Schott J. and Oelkers E. H. (2009) Magnesite growth rates as a function of temperature and saturation state. *Geochim. Cosmochim. Acta* **73**, 5646–5657.

Saldi G. D., Schott J., Pokrovsky O. S. and Oelkers E. H. (2010) An experimental study of magnesite dissolution rates at neutral to alkaline conditions and 150 and 200 °C as a function of pH, total dissolved carbonate concentration, and chemical affinity. *Geochim. Cosmochim. Acta* **74**, 6344–6356.

Saldi G. D., Schott J., Pokrovsky O. S., Gautier Q. and Oelkers E. H. (2012) An experimental study of magnesite precipitation rates at neutral to alkaline conditions and 100–200 °C as a function of pH, aqueous solution composition and chemical affinity. *Geochim. Cosmochim. Acta* **83**, 93–109.

Scheibe T. D., Fang Y., Murray C. J., Roden E. E., Chen J., Chien Y.-J., Brooks S. C. and Hubbard S. S. (2006) Transport and biogeochemical reaction of metals in a physically and chemically heterogeneous aquifer. *Geosphere* **2**. http://dx.doi.org/10.1130/GES00029.1.

Schnoor J. L. (1990) Kinetics of chemical weathering: a comparison of laboratory and field weathering rates. In *Aquatic Chemical Kinetics* (ed. W. Stumm). John Wiley & Sons, Inc., New York.

Shariatpanahi S. F., Strand S. and Austad T. (2011) Initial wetting properties of carbonate oil reservoirs: effect of the temperature and presence of sulfate in formation water. *Energy Fuels* **25**, 3021–3028.

Singha K., Li L., Day-Lewis F. D. and Regberg A. B. (2011) Quantifying solute transport processes: are chemically "conservative" tracers electrically conservative? *Geophysics* **76**, F53–F63.

Sjoberg E. L. and Rickard D. (1983) The influence of experimental design on the rate of calcite dissolution. *Geochim. Cosmochim. Acta* **47**, 2281–2285.

Song X. and Seagren E. A. (2008) In situ bioremediation in heterogeneous porous media: dispersion-limited scenario. *Environ. Sci. Technol.* **42**, 6131–6140.

Steefel C. I. (2007) Geochemical kinetics and transport. In *Kinetics of Water–Rock Interaction* (eds. S. Brantley, J. Kubicki and A. White). Springer.

Steefel C. I., DePaolo D. J. and Lichtner P. C. (2005) Reactive transport modeling: an essential tool and a new research approach for the Earth Sciences. *Earth Planet. Sci. Lett.* **240**, 539–558.

Steefel C. I. and Maher K. (2009) Fluid–rock interaction: a reactive transport approach. *Rev. Mineral. Geochem.*

Steefel C. I. and Van Cappellen P. (1990) A new kinetic approach to modeling water–rock interaction: the role of nucleation, precursors, and Ostwald ripening. *Geochim. Cosmochim. Acta* **54**, 2657–2677.

Swoboda-Colberg N. G. and Drever J. I. (1993) Mineral dissolution rates in plot-scale field and laboratory experiments. *Chem. Geol.* **105**, 51–69.

Tompson A. F. B. and Gelhar L. W. (1990) Numerical-simulation of solute transport in 3-dimensional, randomly heterogeneous porous-media. *Water Resour. Res.* **26**, 2541–2562.

Tompson A. F. B., Schafer A. L. and Smith R. W. (1996) Impacts of physical and chemical heterogeneity on cocontaminant transport in a sandy porous medium. *Water Resour. Res.* **32**, 801–818.

Velbel M. A. (1993) Constancy of silicate-mineral weathering-rate ratios between natural and experimental weathering: implications for hydrologic control of differences in absolute rates. *Chem. Geol.* **105**, 89–99.

Werth C. J., Cirpka O. A. and Grathwohl P. (2006) Enhanced mixing and reaction through flow focusing in heterogeneous porous media. *Water Resour. Res.* **42**.

White A. F. (1995) Chemical weathering rates of silicate minerals in soils. In *Chemical Weathering Rates of Silicate Minerals* (eds. A. F. White and S. L. Brantley). Mineralogical Society of America, Washington, DC.

White A. F. (2002) Determining mineral weathering rates based on solid and solute weathering gradients and velocities: application to biotite weathering in saprolites. *Chem. Geol.* **190**, 69–89.

White A. F. (2008) Quantitative approaches to characterizing natural chemical weathering rates. In *Kinetics of Water–Rock Interaction* (eds. S. L. Brantley, J. D. Kubicki and A. F. White). Springer.

White A. F. and Brantley S. L. (2003) The effect of time on the weathering of silicate minerals: why do weathering rates differ in the laboratory and field? *Chem. Geol.* **202**, 479–506.

White A. F. and Peterson M. L. (1990) Role of reactive-surface-area characterization in geochemical kinetic-models. *ACS Symp. Ser.* **416**, 461–475.

Wilkin R. T., Barnes H. L. and Brantley S. L. (1996) The size distribution of framboidal pyrite in modern sediments: an indicator of redox conditions. *Geochim. Cosmochim. Acta* **60**, 3897–3912.

Willingham T. W., Werth C. J. and Valocchi A. J. (2008) Evaluation of the effects of porous media structure on mixing-controlled reactions using pore-scale modeling and micromodel experiments. *Environ. Sci. Technol.* **42**, 3185–3193.

Wolery T. J., Jackson K. J., Bourcier W. L., Bruton C. J., Viani B. E., Knauss K. G. and Delany J. M. (1990) Current status of the EQ3/6 software package for geochemical modeling. *ACS Symp. Ser.* **416**, 104–116.

Wood B. D. and Whitaker S. (2000) Multi-species diffusion and reaction in biofilms and cellular media. *Chem. Eng. Sci.* **55**, 3397–3418.

Zhang P., Tweheyo M. T. and Austad T. (2006) Wettability alteration and improved oil recovery in chalk: the effect of calcium in the presence of sulfate. *Energy Fuels* **20**, 2056–2062.

Zhu C. (2005) In situ feldspar dissolution rates in an aquifer. *Geochim. Cosmochim. Acta* **69**, 1435–1453.

Zhu C. (2009) Geochemical modeling of reaction paths and networks. In *Thermodynamics and Kinetics of Water–Rock Interactions* (ed. E. H. O. a. J. Schott). Mineralogical Society of America.

Zhu C., Blum A. E. and Veblen D. (2004) Feldspar dissolution rates and clay precipitation in the Navajo aquifer at Black Mesa, Arizona, USA. In *Water–Rock Interaction* (eds. R. B. Wanty and R. R. Seal). A.A. Balkema, Saratoga Springs, New York.

Zinn B., Meigs L. C., Harvey C. F., Haggerty R., Peplinski W. J. and Von Schwerin C. F. (2004) Experimental visualization of solute transport and mass transfer processes in two-dimensional conductivity fields with connected regions of high conductivity. *Environ. Sci. Technol.* **38**, 3916–3926.

Associate editor: Jon Chorover